Proceedings of the
47th IEEE Conference on Decision and Control
Cancun, Mexico, Dec. 9-11, 2008

Recursive Estimation of Terrestrial Magnetic and Electric Potentials

A. M. D'Amato, B. O. S. Teixeira,
H. J. Palanthandalam-Madapusi, A. J. Ridley, D. S. Bernstein

Abstract— **In this paper we recursively estimate the magnetic and electric potential of the Earth's Arctic region. We construct estimates based on data gathered from over 85 magnetometer sources and several radar sites dispersed around the North Pole. The approach to estimating the Arctic polar cap electric potential is through data assimilation based on linear and nonlinear Kalman filters. We demonstrate that the magnetic and electric potential over the Arctic region can be approximately reconstructed from sparse, nonuniform magnetometer and radar data sources.**

I. INTRODUCTION

Our goal is to develop techniques for estimating and forecasting polar region electric and magnetic potential fields. These fields impact society in various ways. For example, large fluctuations in the ionospheric potential can drive large current spikes in municipal power grids. These unexpected currents can overload and destroy power transformers. In fact, in 1989 an extreme event occurred in Quebec, causing a power grid failure that left six million residents without electricity [9]. The ability to predict spikes in ionospheric currents may allow utility suppliers to take action to prevent the destruction of transformers and eliminate power disruption to its customers.

Fluctuations in the ionospheric magnetic potential can also impact satellite systems orbiting the Earth, specifically, the Global Positioning System (GPS). The accuracy of GPS depends on measuring the transit time of signals from Earth-based receivers to the satellites. Fluctuations in the magnetic and electric potential can significantly alter the state of the ionospheric electron density, which subsequently alters the propagation time of these signals and reduces the accuracy of navigation systems.

We use data gathered from magnetometers and radars in northern Canada and northern Europe. As outlined in Table I, a linear Kalman filter (KF) is employed to estimate the magnetic potential. The electric potential is estimated using both a KF and an unscented Kalman filter (UKF).

This research was supported by the National Science Foundation, under grants ATM-0417839 and CNS-0539053 to the University of Michigan, Ann Arbor, USA, and by FAPEMIG and CNPq, Brazil.

Graduate Student, Department of Aerospace Engineering, The University of Michigan, Ann Arbor, MI 48109-2140, email: amdamato@umich.edu.

Post-Doctoral Fellow, Department of Electronic Engineering, TFederal University of Minas Gerais, Belo Horizonte, MG, Brazil, 31270-090, email: brunoot@ufmg.br.

Assistant Professor, Department of Mechanical and Aerospace Engineering, Syracuse University, Syracuse, NY 13244 , email: hjpalant@syr.edu.

Associate Professor, Department of Atmospheric, Oceanic and Space Sciences, The University of Michigan, Ann Arbor, MI 48109-2140.

Professor, Department of Aerospace Engineering, The University of Michigan, Ann Arbor, MI 48109-2140.

TABLE I
DATA ASSIMILATION OUTLINE

	Mag. Data	Radar Data	Both
Magnetic Potential	KF	-	-
Electric Potential	UKF	KF or UKF	UKF

II. MAGNETIC POTENTIAL ESTIMATION MODEL

The Earth's magnetic potential field can be viewed as a set of contours that outline areas of equal potential. To approximate these contours, a grid is constructed from 44° to 90° latitude and from 0 h to 24 h, where 0 h corresponds to the longitude at midnight in a Sun-fixed coordinate frame. Here, latitude and longitude refer to geomagnetic coordinates. Each point of intersection of the grid lines is a pixel of the image. The number of pixels is $n = n_{\rm lat} n_{\rm long}$, where $n_{\rm lat}$ is the number of latitude divisions and $n_{\rm long}$ is the number of longitude divisions . We assemble the data into matrices of size $n_{\rm lat} \times n_{\rm long}$. Specifically, the magnetic potentials are represented by

$$G_{\psi,k} \triangleq \begin{bmatrix} \psi_{\mathrm{lat}_1\mathrm{long}_1} & \cdots & \psi_{\mathrm{lat}_n\mathrm{long}_1} \\ \psi_{\mathrm{lat}_1\mathrm{long}_2} & \cdots & \psi_{\mathrm{lat}_n\mathrm{long}_2} \\ \vdots & \ddots & \vdots \\ \psi_{\mathrm{lat}_1\mathrm{long}_n} & \cdots & \psi_{\mathrm{lat}_n\mathrm{long}_n} \end{bmatrix} \in \mathbb{R}^{n_{\rm lat} \times n_{\rm long}}, \tag{1}$$

where $\psi_{\mathrm{long}_i\mathrm{lat}_i}$ is the magnetic potential ψ at longitude long_i and latitude lat_i. It is convenient to represent $G_{\psi,k}$ as the column vector

$$\Psi_k \triangleq \mathrm{vec}\ G_{\psi,k} \ \in \mathbb{R}^n, \tag{2}$$

where $\Psi_k = [\psi_{k,1} \cdots \psi_{k,n}]^{\mathrm{T}}$. We model the magnetic potential field as a linear discrete-time system of the form

$$x_{k+1} = A_k x_k + w_k, \tag{3}$$

$$y_k = C_k x_k + v_k, \tag{4}$$

where $x_k = \Psi_k$ is the magnetic potential field at time k. Since the model is assumed to be static, the transition matrix $A_k \in \mathbb{R}^{n \times n}$ is given by

$$A_k = I. \tag{5}$$

Furthermore, $w_k \in \mathbb{R}^n$ represents the effects of disturbances on the magnetic field, $y_k \in \mathbb{R}^q$ is the vector of sensor measurements, and $v_k \in \mathbb{R}^q$ is the measurement noise. Therefore $C_k \in \mathbb{R}^{q \times n}$. Henceforth we drop the time index k for simplicity.

978-1-4244-3124-3/08/$25.00 ©2008 IEEE

The components of y are the ground magnetic field perturbation readings, obtained from over 85 magnetometers. These magnetometers are roughly globally distributed over land masses. Only magnetometers poleward of 50° magnetic latitude are utilized in this study. It should be noted that magnetic and geographic latitude are different, since the magnetic north pole is 11° south of the geographic north pole toward Canada.

To estimate the ground magnetic potential field $\vec{B}_{\rm g}$, the magnetic potential field perturbation readings are assumed to approximate the magnetic potential gradient given by

$$\vec{B_{\rm g}} = \nabla\psi. \tag{6}$$

Each magnetometer measures field perturbations in three directions, namely, vertical, north, and east of the Earth-fixed frame at the magnetometer's location. In spherical coordinates, $\vec{B}_{\rm g}$ is given by

$$\vec{B_{\rm g}} = \frac{\partial\psi}{\partial r}\,\hat{r} + \frac{1}{R_{\rm e}}\frac{\partial\psi}{\partial\theta}\,\hat{\theta} + \frac{1}{R_{\rm e}\sin\theta}\frac{\partial\psi}{\partial\phi}\,\hat{\phi}, \tag{7}$$

where $\hat{r}$, $\hat{\theta}$, and $\hat{\phi}$ are unit vectors in the vertical, northerly and easterly directions, respectively, and $R_{\rm e}$ is the radius of the Earth. Furthermore, we define $\Theta \triangleq \text{vec}\ G_\theta \in \mathbb{R}^n$ and $\Phi \triangleq \text{vec}\ G_\phi \in \mathbb{R}^n$ analogously to (1), where θ and ϕ are latitude and longitude, respectively.

Letting $q_{\rm E}$ and $q_{\rm N}$ represent the number of east and north measurements, respectively, the observation matrix can be represented as

$$C = \begin{bmatrix} C_{\rm E} \\ C_{\rm N} \end{bmatrix},$$

where $C_{\rm E} \in \mathbb{R}^{q_{\rm E}\times n}$ and $C_{\rm N} \in \mathbb{R}^{q_{\rm N}\times n}$. The vertical direction measurements are not used. For $i = 1,\ldots,q_{\rm E}$, the entries of C corresponding to an easterly sensor measurement $y_{{\rm E},i}$ located at pixel j are

$$C_{i,j+n_{\rm lat}} = \frac{1}{2R_{\rm e}(\sin\Theta_j)(\Phi_{j+n_{\rm lat}} - \Phi_j)}, \tag{8}$$

$$C_{i,j-n_{\rm lat}} = \frac{-1}{2R_{\rm e}(\sin\Theta_j)(\Phi_{j-n_{\rm lat}} - \Phi_j)}, \tag{9}$$

For $i = q_{\rm E}+1,\ldots,q_{\rm E}+q_{\rm N}$, the entries of C corresponding to a northerly measurement $y_{{\rm N},i}$ located at pixel j are

$$C_{i,(j-1)} = \frac{1}{2R_{\rm e}(\Theta_{j-1} - \Theta_j)}, \tag{10}$$

$$C_{i,(j+1)} = \frac{-1}{2R_{\rm e}(\Theta_{j+1} - \Theta_j)}. \tag{11}$$

A. LINEAR KALMAN FILTER

Since the observations y_k are linear functions of the magnetic potential field we use the KF to estimate the magnetic potential over the grid. A forecast estimate $x^{\rm f}_{k+1}$ and forecast error covariance $P^{\rm f}_{k+1}$ at time $k+1$ are defined as

$$x^{\rm f}_{k+1} = A_k x^{\rm da}_k, \tag{12}$$

$$P^{\rm f}_{k+1} = A_k P^{\rm da}_k A^T + Q, \tag{13}$$

where Q is the process noise covariance and $P^{\rm da}_k$ is the error covariance at time k. For the data assimilation step, the data injection gain K is

$$K_{k+1} = P^{\rm f}_{k+1}C^T_{k+1}(C_{k+1}P^{\rm f}_{k+1}C^T_{k+1} + R)^{-1}, \tag{14}$$

where R is the measurement noise covariance. The data assimilation step is

$$x^{\rm da}_{k+1} = x^{\rm f}_{k+1} + K_{k+1}(y_{k+1} - C_{k+1}x^{\rm f}_{k+1}). \tag{15}$$

The error covariance is updated by

$$P^{\rm da}_{k+1} = (I - K_{k+1}C_{k+1})P^{\rm f}_{k+1}. \tag{16}$$

Two diagnostics are used to assess the KF performance. The mean standard deviation of the error, which is obtained from the error covariance matrix, is analyzed. Next, the measurement residual is examined. Acceptable performance occurs when the measurement residual $y_k - \hat{y}_k$ is within ± 3 $\sigma_{y,k}$, where

$$\sigma_{y,k} \triangleq \sqrt{C_{k+1}P^{\rm f}_{k+1}C^T_{k+1} + R} \tag{17}$$

is the measurement error standard deviation for a sensor y at time k.

B. MAGNETIC POTENTIAL ESTIMATION

The model parameters are initialized with data from May 1st 1998 from 00:00 to 23:59 UT. The optimal Kalman filter presented in Section II-A is based on error covariance Q and measurement covariance R. These values are not known and must be estimated to use the KF. We introduce the estimated error covariance $\hat{Q}$ and estimated measurement covariance $\hat{R}$. In particular, $\hat{Q}$ is estimated by scaling the electric potential covariance taken from the assimilative mapping of ionospheric electrodynamics (AMIE) data sources [8]. Furthermore, $\hat{R}$ is chosen to be a diagonal matrix with entries $\hat{R}_{i,i} = \sigma^2{}_{y_i}$, where σ_{y_i} is the standard deviation of the measurement y_i for the sampled time period. The initial error covariance matrix P is chosen to be a diagonal matrix with entries $P_{i,i} = 10^4$. Choices for $\hat{Q}$, $\hat{R}$ and $\hat{P}$ are determined and adjusted based on the results of the filter diagnostics.

The KF is used to assimilate the magnetometer data, yielding an image of the polar magnetic potential as shown in Figure 1(a). The black circles are the magnetometer locations at 06:00 Z UT. Dominant high and low areas can be observed in the image. Figure 2 shows the trace of the error covariance matrix from 00:00 to 23:59 Z UT. The error approaches steady state at approximately 100 minutes after midnight. The final diagnostic is the analysis of the measurement residual over the time period. Figures 3 and 4 show measurement residual plots from two different sensors. The measurement residuals are within ± 3 standard deviations of measurement residual error. In the absence of true magnetic potential values for comparison, the diagnostics and images are used to detect anomalous estimation errors.

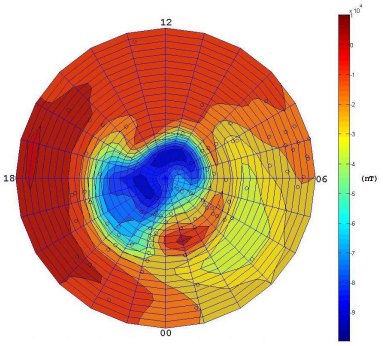

(a) Magnetic Field May 1, 1998 6h:00 Z

Fig. 1. Polar magnetic potential field. Dominant high and low areas can be seen in the image. The black circles indicate magnetometer locations at this time period.

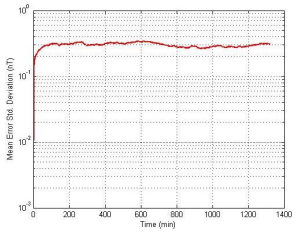

Fig. 2. Mean error standard deviation. The standard deviation starts to converge at about 100 minutes past midnight on May 1st 1998.

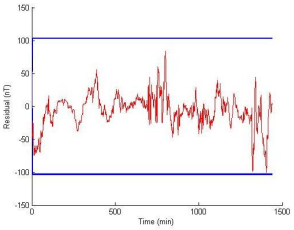

(a)

Fig. 3. Example of easterly measurement residual.

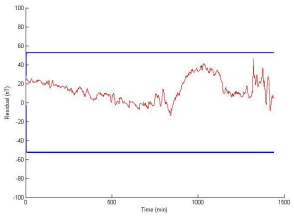

(a)

Fig. 4. Example of northerly measurement residual.

III. ELECTRIC POTENTIAL ESTIMATION MODEL

The electric potential field is estimated with the same method used for the magnetic potential field. The measurements for estimating the polar electric potential are drift velocity readings from the SuperDARN radar network [6] and magnetometer readings from AMIE. The model used for electric potential is similar to the one presented in Section II. Three methods for electric potential estimation are presented, a linear KF with drift velocity measurements, the UKF with magnetometer measurements, and the UKF with drift velocity and magnetometer measurements.

We use the discrete-time linear model (3),(4) with the state vector x_k redefined as the electric potential at each pixel. To construct an observation matrix we introduce drift velocity measurements $\vec{V}$, which are related to the electric field $\vec{E}$ by

$$\vec{V} = \frac{\vec{E} \times \vec{B}}{B^2} \in \mathbb{R}^3, \tag{18}$$

where $\vec{B}$ is the magnetic field of the earth. The data for $\vec{B} = [B_r \ B_\theta \ B_\phi]^T$ is generated using the International Geomagnetic Reference Field (IGRF). The electric field is related to the electric potential ψ by

$$\vec{E} = -\nabla\psi. \tag{19}$$

The drift velocity in spherical coordinates is therefore

$$\begin{aligned}\vec{V} &= \frac{1}{B^2}\left(\frac{B_\theta \partial\psi}{R_\mathrm{e}\sin\theta\partial\phi} - \frac{B_z\partial\psi}{R_\mathrm{e}\partial\theta}\right)\hat{r} \\ &+ \frac{1}{B^2}\left(\frac{B_\phi\partial\psi}{\partial r} - \frac{B_r\partial\psi}{R_\mathrm{e}\sin\theta\partial\phi}\right)\hat{\theta} \\ &+ \frac{1}{B^2}\left(\frac{B_r\partial\psi}{R_\mathrm{e}\partial\theta} - \frac{B_\theta\partial\psi}{\partial r}\right)\hat{\phi}\end{aligned}$$

where R_e is the radius of the Earth and $\hat{r}$, $\hat{\theta}$, $\hat{\phi}$ are unit vectors in the vertical, northerly, easterly directions respectively. The radars measure flow toward or away from their location, that is, a line-of-sight measurement, as described by [2]. Each line-of-sight measurement intersects the local longitude at an angle α, such that the measurements are scalar values, where

$$V = \sin\alpha\left(\frac{B_r}{B^2R_\mathrm{e}}\frac{\partial\psi}{\partial\theta} - \frac{B_\theta}{B^2}\frac{\partial\psi}{\partial r}\right) + \cos\alpha\left(\frac{B_\phi}{B^2}\frac{\partial\psi}{\partial r} - \frac{B_r}{B^2R_\mathrm{e}\sin\theta}\frac{\partial\psi}{\partial\phi}\right). \tag{20}$$

Because magnetic fields are primarily radial in the polar ionosphere, and ψ is constant along magnetic field lines, terms involving $\frac{\partial}{\partial r}$ are neglected. The discrete velocity components are derived to create $C \in \mathbb{R}^{q\times n}$. For $i = 1, \ldots, q$, the entries of C corresponding to an easterly drift velocity measurement y_i at pixel j are

$$C_{i,(j+n_\mathrm{lat})} = \frac{B_r\cos\alpha}{2B^2R_\mathrm{e}\sin\Theta_j(\Phi_{j+n_\mathrm{lat}} - \Phi_i)}, \tag{21}$$

$$C_{i,(j-n_\mathrm{lat})} = \frac{-B_r\cos\alpha}{2B^2R_\mathrm{e}\sin\Theta_j(\Phi_{j-n_\mathrm{lat}} - \Phi_i)}. \tag{22}$$

For the same measurement y_i, the northerly measurements are

$$C_{i,(j-1)} = \frac{-B_r\sin\alpha}{2B^2R_\mathrm{e}(\Theta_{j-1} - \Theta_j)}, \tag{23}$$

$$C_{i,(j+1)} = \frac{B_r\sin\alpha}{2B^2R_\mathrm{e}(\Theta_{j+1} - \Theta_j)}. \tag{24}$$

The electric potential is estimated using the same KF presented in Section II-A. However, the data provided by SuperDARN includes measurement standard deviation.

A. LINEAR ELECTRIC POTENTIAL ESTIMATION

The model parameter Q is initialized with data from May 1st 1998 from 00:00 to 08:20 UT, with Q estimated by scaling the electric potential covariance taken from AMIE data sources. R is provided from the SuperDARN data.

The error standard deviation in Figure 5 indicates stable performance, approaching a steady state value at approximately 100 minutes after midnight. The image shown in

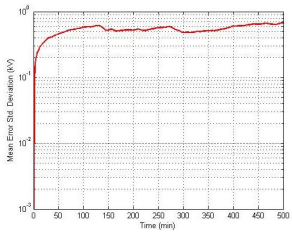

Fig. 5. The mean error standard deviation. The standard deviation indicates that the filter reaches a steady state before the end of the time interval.

Figure 6(a) is generated with the Kalman filter and is compared to the image generated from the AMIE technique [8]. AMIE is used as a benchmark for filter performance. The image generated for May 1st shows a valid electric potential pattern, the high and low area coincide with the AMIE image. Error in potential pattern trends is shown by the magnitude

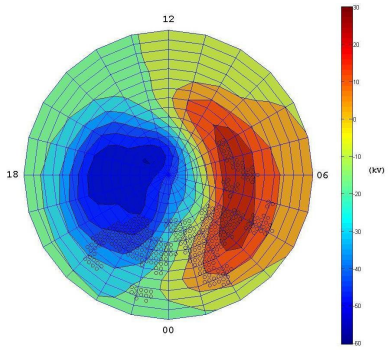

(a) KF estimated polar electric potential field.

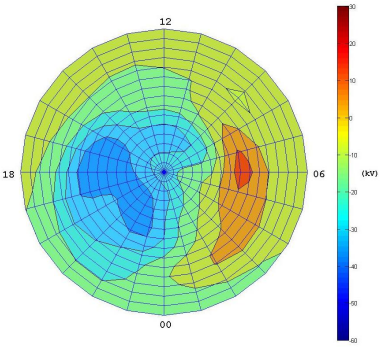

(b) AMIE estimated electric potential.

Fig. 6. The images are generated for May 1, 1998 5h:00 Z.

of the cross polar potential difference, which is the difference between the absolute high and absolute low of the electric potential field. The cross polar difference for AMIE and the KF estimate are shown in Figure 7. Observing the potential

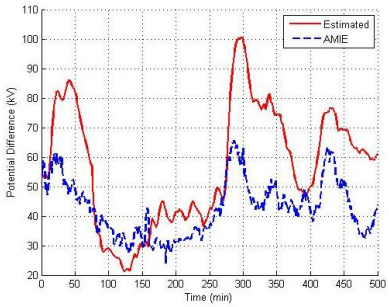

Fig. 7. The cross polar potential difference is used to determine if the estimates are producing the correct electric potential trends. We use this diagnostic to detect filter divergence.

difference and error covariance suggests that the KF produces acceptable estimates from 01:00 Z to about 04:30 Z UT. After this time the KF does not track the potential difference well. Note that the SuperDARN measurements are localized to a small area of the grid as shown in Figure 6(a), where the black circles indicate radar locations.

IV. NONLINEAR ELECTRIC POTENTIAL MODEL

To use the magnetometer data for electric potential estimation we consider the nonlinear discrete-time model

$$x_{k+1} = A_k x_k + w_k, \tag{25}$$

$$y_k = H(x_k) + v_k, \tag{26}$$

where A_k, x_k, w_k, v_k are defined in Section II. $H(\cdot)$ is a nonlinear observation function used to relate magnetometer measurements to the electric potential. Since the KF presented in Section II-A cannot be used for this system, we use the UKF. To obtain $H(\cdot)$ we start from the current density $\vec{J_H} = [J_r \ J_\theta \ J_\phi]^{\mathrm{T}}$ of the polar region, which is

$$\vec{J_H} = \frac{-\sigma_H \nabla\psi \times \vec{B}}{|B|}, \tag{27}$$

where σ_H is the hall conductance [3]. The current density is related to the magnetometer measurements $\vec{B}_{\mathrm{g}}$ by

$$\vec{B}_{\mathrm{g}} = \frac{\mu_0}{4\pi} \int \frac{\vec{J_H} \times \vec{\rho}}{\rho^3} dA, \tag{28}$$

where μ_0 is the permeability of free space. The position of the current source relative to the magnetometer location is $\vec{\rho} = [\rho_r \ \rho_\theta \ \rho_\phi]^{\mathrm{T}}$. Evaluating the cross product in (27) gives

$$\vec{B}_{\mathrm{g}} = \frac{\mu_0}{4\pi} \int \left(\frac{J_\theta \rho_\phi - J_\phi \rho_\theta}{\rho^3} \hat{r} + \frac{J_\phi \rho_r - J_r \rho_\phi}{\rho^3} \hat{\theta} + \frac{J_r \rho_\theta - J_\theta \rho_r}{\rho^3} \hat{\phi} \right) dA. \tag{29}$$

The three components of $\vec{B}_{\mathrm{g}} = [B_{g_z} \ B_{g_\theta} \ B_{g_\phi}]^{\mathrm{T}}$ for a magnetometer $m = 1, \ldots, q$ are

$$B_{\mathrm{g}_{z\,m}} = \sum_{j=1}^{n_{\mathrm{lat}}} \sum_{i=1}^{n_{long}} \frac{\mu_0}{4\pi} \left[\frac{J_{\theta\,i,j} \rho_{\phi\,i,j} - J_{\phi\,i,j} \rho_{\theta\,i,j}}{\rho_{i,j}^3} \right] R_{\mathrm{e}}^2 \sin G_{\theta,k_{i,j}} \Delta\theta \Delta\phi, \tag{30}$$

$$B_{g_{\theta\, m}} = \sum_{j=1}^{n_{lat}} \sum_{i=1}^{n_{long}} \frac{\mu_0}{4\pi} \left[\frac{J_{\phi\, i,j}\rho_{r\, i,j} - J_{r\, i,j}\rho_{\phi\, i,j}}{\rho_{i,j}^3} \right] R_e^2 \sin G_{\theta,k\, i,j} \Delta\theta\Delta\phi, \quad (31)$$

$$B_{g_{\phi\, m}} = \sum_{j=1}^{n_{lat}} \sum_{i=1}^{n_{long}} \frac{\mu_0}{4\pi} \left[\frac{J_{r\, i,j}\rho_{\theta\, i,j} - J_{\theta\, i,j}\rho_{r\, i,j}}{\rho_{i,j}^3} \right] R_e^2 \sin G_{\theta,k\, i,j} \Delta\theta\Delta\phi, \quad (32)$$

where $\Delta\theta$ and $\Delta\phi$ are the dimensions of the unit area we use to numerically integrate these components.

A. UNSCENTED KALMAN FILTER

To implement the UKF choose $2n+1$ sigma points, where n is the number of states, given by

$$\begin{aligned} \hat{x}_k^{(i)} &= \hat{x}_k + \left(\sqrt{(n+\lambda)P_k}\right)_i^{\mathrm{T}} \quad i = 1, \ldots, n, \\ \hat{x}_k^{(n+i)} &= \hat{x}_k - \left(\sqrt{(n+\lambda)P_k}\right)_i^{\mathrm{T}} \quad i = 1, \ldots, n, \end{aligned}$$

where P_k is the error covariance and $\lambda = \alpha^2(n+\kappa) - n$. We also create two weighting vectors

$$\begin{aligned} W_s^{(i)} = W_c^{(i)} &= \tfrac{1}{2(n+\lambda)}, \\ W_s^{(0)} &= \tfrac{\lambda}{n+\lambda}, \\ W_c^{(0)} &= \tfrac{\lambda}{n+\lambda} + (1 - \alpha^2 + \beta), \end{aligned}$$

where W_s weights state estimates and W_c weights covariance estimates. We obtain the forecast estimate by summing the weighted sigma points

$$x^{\mathrm{f}}{}_{k+1} = \frac{1}{2n} \sum_{i=1}^{2n} W_s^{(i)} x_k{}^{(i)}. \quad (33)$$

We obtain the state forecast directly from the weighted sigma points because the model is static. The weighted forecast error covariance is obtained from

$$P^{\mathrm{f}}{}_{k+1} = \frac{1}{2n} \sum_{i=1}^{2n} W_c^{(i)} \left(\hat{x}_{k+1}^{(i)} - \hat{x}^f\right) \left(\hat{x}_{k+1}^{(i)} - \hat{x}^f\right)^{\mathrm{T}} + Q, \quad (34)$$

where Q is the process noise covariance. We then transform the sigma points into a vector of predicted measurements by using $H(\cdot)$ such that

$$\hat{y}_{k+1}^{(i)} = H\left(\hat{x}_{k+1}^{(i)}, k\right), \quad (35)$$

where $H(\cdot)$ is (30),(31),(32). The predicted measurements are weighted and combined to recover the measurement estimate $\hat{y}_{k+1}$, where

$$\hat{y}_{k+1} = \frac{1}{2n} \sum_{i=1}^{2n} W_s^{(i)} \left(\hat{y}_{k+1}^{(i)}\right). \quad (36)$$

The estimated measurement covariance P_y and the state measurement cross covariance P_{xy} is

$$\begin{aligned} P_{y_{k+1}} &= \tfrac{1}{2n} \sum_{i=1}^{2n} W_c^{(i)} \left(\hat{y}_{k+1}^{(i)} - \hat{y}_{k+1}\right) \left(\hat{y}_{k+1}^{(i)} - \hat{y}\right)^{\mathrm{T}} + R, \\ P_{xy_{k+1}} &= \tfrac{1}{2n} \sum_{i=1}^{2n} W_c^{(i)} \left(\hat{x}_{k+1}^{(i)} - \hat{x}^f\right) \cdot \left(\hat{y}_{k+1}^{(i)} - \hat{y}\right)^{\mathrm{T}}, \end{aligned}$$

where R is the estimated measurement covariance. The data assimilation step requires a data injection gain K based on P_y and P_{xy}. The gain K is

$$K_{k+1} = P_{xy_{k+1}} P_{y_{k+1}}^{-1}. \quad (37)$$

The state estimate and error covariance are

$$\begin{aligned} x_{k+1}^{\mathrm{da}} &= x_{k+1}^{\mathrm{f}} + K_{k+1}(y_{k+1} - \hat{y}_{k+1}), \\ P_{k+1}^{\mathrm{da}} &= P_{k+1}^{f} - K_{k+1} P_{y_{k+1}} K_{k+1}^{\mathrm{T}}. \end{aligned}$$

To determine filter performance we analyze the mean standard deviation of the error, as in Section II-A. Electric potential data is available from AMIE for this time period and resolution, which we use to assess candidate values for $\hat{Q}$ and $\hat{R}$.

B. NONLINEAR ESTIMATION

The model parameters are initialized with data from May 1st 1998 from 00:00 to 08:20 Z UT, with Q estimated by scaling the electric potential covariance taken from AMIE data sources. The measurement covariance is

$$R = \begin{bmatrix} R_{\mathrm{d}} & 0 \\ 0 & R_{\mathrm{m}} \end{bmatrix},$$

where R_{d} is the measurement covariance for the drift velocity measurements from Section IV and R_{m} is the estimated magnetometer covariance from Section II-B. The Kalman filter parameters κ, α, and β are initialized as 0, 1, 2, respectively.

The error standard deviation for magnetometer only, as well as with both data sets show that the filter approaches steady state at about 75 minutes after midnight. The cross

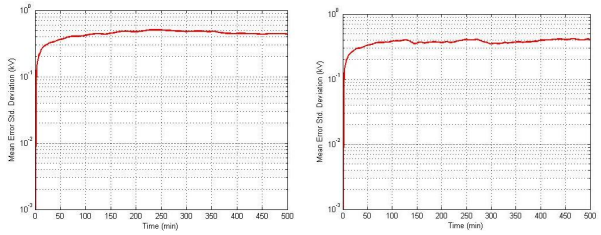

(a) Mean error standard deviation, magnetometer data only. (b) Mean error standard deviation, radar and magnetometer data.

Fig. 8. Mean error standard deviation analysis. In both cases, the mean error standard deviation reaches steady state approximately 75 minutes after midnight.

polar potential difference plots in Figure 9 show comparable estimates to AMIE. When compared to the linear filter with radar data only (Figure 7) the linear filter does not follow AMIE's trends 300 minutes past midnight. However, the UKF and combined data UKF provide acceptable tracking for the entire simulation. The polar images generated for May 1 1998, show valid electric potential patterns. The locations of the highs and lows are within the expected range and locations. Figures 10(a) and 10(b) are polar images generated using the unscented Kalman filter. Figure 10(a) is an image based on magnetometer data, and Figure 10(b) is based on combined radar and magnetometer data. Figure 10(c) is generated from AMIE data for comparison. The diagnostics performed on the UKF, namely, the cross polar

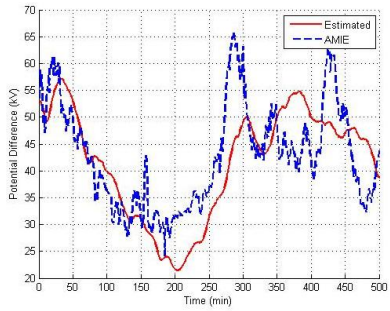

(a) Cross polar potential difference, magnetometer data only.

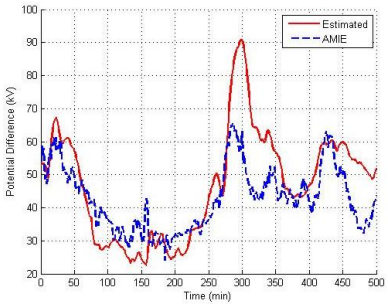

(b) Cross polar potential difference, radar and magnetometer data.

Fig. 9. Both UKF's show good estimations of the cross polar potential difference. The UKF with combined data in Figure 9(b) shows acceptable tracking for the entire time period.

potential difference show that the nonlinear estimation better estimates the electric potential field than its linear counterpart in Section III.

V. Conclusion

Using magnetometer and drift velocity measurements, the polar magnetic and electric potentials were estimated using linear and nonlinear Kalman filters. The magnetic and electric potential fields were set up as linear discrete-time systems, driven by external disturbances. Linear expressions were used to relate magnetometer and drift velocity measurements to the magnetic and electric potential fields, respectively. Furthermore, the electric potential was also set up as a nonlinear discrete-time system, driven by external disturbances. A nonlinear function was used to relate the magnetometer measurements to the electric potential field. The nonlinear filter was used with magnetometer measurements, and with combined drift velocity and magnetometer data. Results were demonstrated using real data.

References

[1] D. Simon, *Optimal State Estimation*, 1st Edition, Wiley Publishing, 2006.

[2] H.J. Palanthandalam-Madapusi, S. Gillijns,A. J. Ridley, D. S. Bernstein, , B. De Moor, "Electric Potential Estimation with Line-of-Sight Measurements Using Basis Function Optimization," *42nd IEEE Conf on Decision and Control*, Atlantis, Paradise Island, Bahamas, pp. 3625-3630, December 2004

[3] J. D. Griffiths, *Introduction to Electrodynamics*, Second Edition, Prentice-Hall, 1989.

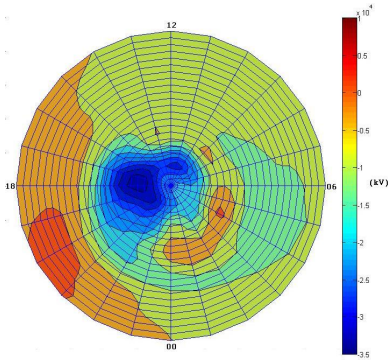

(a) Magnetometer estimated electric field

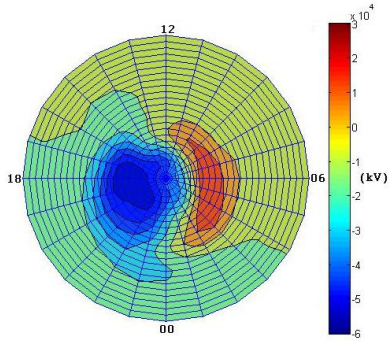

(b) Radar and magnetometer estimated electric field

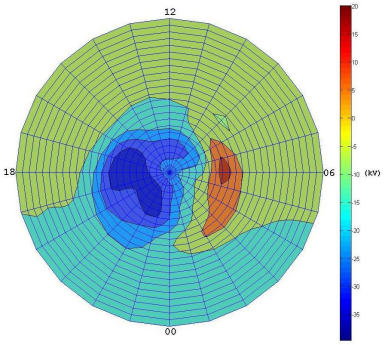

(c) AMIE estimated electric field

Fig. 10. Figures 10(a) and 10(b) are polar images generated using the unscented Kalman filter. Figure 10(c) is generated by AMIE. All data is for May 1, 1998 5h:00 Z

[4] D. S. Bernstein, *Matrix Mathematics*, Princeton University Press, 2005.

[5] B. D. O. Anderson, J. B. Moore, *Optimal Filtering*, Dover Publications, 2005.

[6] J.M. Ruohoniemi, R.A. Greenwald, "Statistical patterns of the high-latitude convection obtained from Goose Bay HF radar observations," *J. Geophys. Res.*, V101, N1, pp. 21-743, 1996

[7] J. J. Love, "Magnetic Monitoring of Earth and Space", *Physics Today*, pp. 31-37, Feburuary 2008

[8] A. D. Richmond, "Assimilative Mapping of Ionospheric Electrodynamics", *Adv. Space Res.*, Vol. 12, No. 6,pp. (6)59-(6)68, 1992.

[9] United States Geological Survey. "USGS Reports Geomagnetic Storm In Progress", ScienceDaily, 28 August 1998. 9 March 2008, http://www.sciencedaily.com /releases/1998/08/980828074001.htm.